On the Redox Activity of the Solid Electrolyte Interphase in the Reduction/Oxidation of Silicon Nanoparticles in Secondary Lithium Batteries

Corrado Bongiorno, Giovanni Mannino,* Umberto D'Alessio, Francesca Monforte, Guglielmo Guido Condorelli, Corrado Spinella, Antonino La Magna, and Sergio Brutti

Chemical and structural modifications occurring in homogeneous crystalline Si nanoparticles (NPs) used as anode material in Li cells are investigated. State-of-the-art high-resolution scanning transmission electron microscopy coupled with electron energy loss spectroscopy resolved at the nanoscale is exploited. It is directly highlighted by electron spectromicroscopy that, above 0.1 V versus Li, the electrochemical activity of Si electrodes involves a complex interplay between Li incorporation, electrolyte degradation, and Si reduction/oxidation. These redox processes occur upon cycling through partially reversible reactions mediated by the solid electrolyte interphase. Overall, a SiO_2 amorphous layer forms in the oxidized electrodes at the Si NPs interface with the electrolyte: this oxide shell partially dissolves upon reduction to give Li_2CO_3 and amorphous Si. Si NPs cores are therefore eroded upon cycling as their outer layers are directly involved in a reversible oxygen shifting mechanism at the interface, whereas unreacted SiO_2 accumulates cycle-by-cycle. These findings extend the comprehension of the Si pulverization mechanism in Li batteries.

C. Bongiorno, G. Mannino, C. Spinella, A. La Magna
CNR-IMM
Strada VIII n°5 Zona Industriale
95121 Catania, Italy
E-mail: giovanni.mannino@imm.cnr.it

U. D'Alessio, S. Brutti
Dipartimento di Chimica
Università degli Studi di Roma "La Sapienza" and INSTM UdR Roma
00185 Roma, Italy

F. Monforte, G. G. Condorelli
Dipartimento di Scienze Chimiche
Università di Catania and INSTM UdR Catania
95125 Catania, Italy

S. Brutti
CNR-ISC
UOS Sapienza via dei Taurini
00185 Roma, Italy

1. Introduction

Li-ion batteries are leading power sources for portable electronics.[1] Despite the enormous resources spent in recent years to extend their application to the electric vehicles (EVs) market,[2,3] performance, cost, and safety limitations slow down their massive adoption to substitute traditional combustion engine cars. A higher penetration of Li-ion technology in the automotive and on grid storage applications would benefit by the substitution of the currently used negative electrode material, namely graphite with theoretical capacity of $372 \, mAh \, g^{-1}$,[4] with higher energy density active materials such as pyrolytic carbon ($4–500 \, mAh \, g^{-1}$),[5] graphene ($750 \, mAh \, g^{-1}$)[6] and black phosphorous ($2400 \, mAh \, g^{-1}$)[7] or other Li alloying elements like Sn, Al, and Ge.[8] In particular, Si can supply a high theoretical gravimetric capacity of $3579 \, mAh \, g^{-1}$, relative to the Li-richest crystalline phase $Li_{15}Si_4$,[9] and an operational potential below 0.5 V versus Li.[10] Nevertheless, the use of bulk Si as alloying negative electrode implies significant volume variations (larger than 300%)[11] upon Li insertion/extraction, leading to quick mechanical failure of the active material, loss of electronic contacts among particles and solid electrolyte interphase (SEI) instability. Therefore, Si negative electrodes suffer from poor cyclability due to the rapid fading in electrochemical performances occurring in parallel with the rise of internal cell resistivity.[10,12] Many strategies have been proposed to mitigate volume expansion and, in turn, prevent or retard Si particle fracturing. Among these strategies, the use of nanostructured Si is one of the most mature,[10–17] levering on the increased elasticity of nanostructures and the 3D expansion capability.[18,19]

It is nowadays accepted that silicon particles below 100 nm, or nanowires with diameters below 50–100 nm, well counteract the cyclic volume variation upon lithiation/delithiation with increasing the cell lifetime.[12,13] However, despite the improved capacity retention upon cycling compared to bulk, also in the case of nanostructured Si anodes cell performances fade upon repeated electrochemical Li loading/unloading, due to the apparently inevitable pulverization of primary particles in few tenths of cycles.[20]

The understanding of Si NPs structural degradation pathway during lithiation/delithiation processes is widening thanks to new generation scanning transmission electron microscopes

(STEM).[18,21] In recent years, detailed STEM analyses described the morphological evolution of Si NPs collected postmortem after galvanostatic cycles in Li cells.[22–25] STEM highlighted a Si dendritization ending in a complete pulverization. After the complete dendritization, a change in the degradation mechanism has been proposed to explain the inevitable speed up in the performance deterioration.[21,26] On the other hand, only few examples of the analysis at the nanoscale of the composition evolution upon cycling of Si electrodes have been reported so far.[23,24]

Si pulverization results from the lithiation of Si NPs to form at potential below 0.05 V versus Li^+/Li the highly lithiated $Li_{15}Si_4$ phase.[27–29] Its formation expands the Si lattice of more than 300%, thus leading to the incorporation of extended defects, cracks, and fragmentation of the primary Si NPs. A common strategy to mitigate this detrimental effect and improve the cyclability of Si electrodes is to limit the cathodic potential cutoff to prevent the formation of the $Li_{15}Si_4$ phase.[9,10,23,24] Overall, the potential limitation decreases the total lithiation capacity and increases the reversibility/calendar life of the cells. However even in silicon electrodes with cathodic potential cutoffs above 0.1 V versus Li, primary particles pulverization is observed, thus implying the occurrence of additional degradation mechanisms.[20–23]

Like in all negative electrodes of aprotic lithium batteries, the solid electrolyte interphase (SEI) plays a key role for Si electrodes.[30–33] Most common SEI observed in Si anodes are composed of inorganic lithium carbonates or lithium fluorides together with other organic compounds.[34,35] Upon cycling silicon electrodes, the SEI growths and dissolves, in interstices and pores, generating large mixed agglomerates[20,21,23–26,36] and suffering relevant thickness breaths.[18,21,26,37] These morphological variations have been related to precipitation of lithium carbonate and C layers in the SEI over Si nanowires,[19,25,30,38,39] as well as the formation of SiO_x phases on the surface of the Si NPs.[40–44] This complex reactivity implies an evident redox activity of the SEI thus raising new questions about the extent of the Li–Si alloying charge storage mechanism.

Here, we tackle the challenge to demonstrate experimentally the alteration of the morphology and composition of crystalline silicon nanoparticles (Si NPs) upon cycling in aprotic electrochemical cells. To reach this aim, we exploit state-of-the-art high-resolution scanning transmission electron microscopy (TEM) coupled with electron energy loss spectroscopy resolved at the nanoscale.

2. Results

The anode Si-based material is constituted by crystalline Si NPs obtained by chemical vapor deposition (CVD). The characterization of Si NPs is shown in the Supplementary Note 1. It is composed of octahedral Si NPs with a sharp size distribution around 150 nm. Raman spectra reveals the presence of 30% of amorphous Si, likely layered on the crystalline core of the Si NPs (see **Figure 1**c and S1c, Supporting Information). Starting from this material, composite electrodes have been manufactured following the procedures described in the Experimental Section.
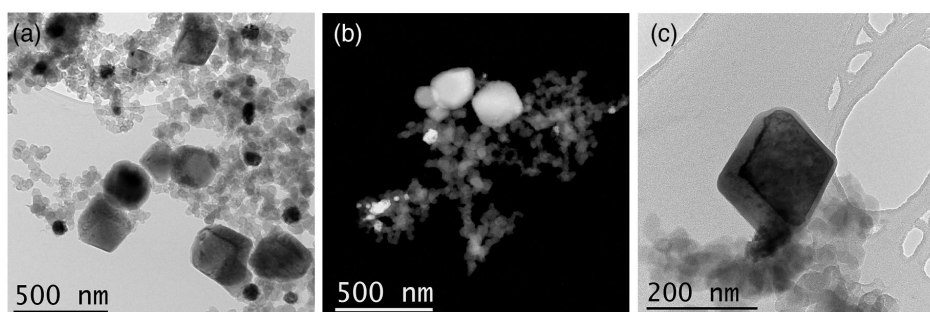
In Figure 1, we show the as-prepared electrode blend, which is composed of two main components: Si NPs and round-shaped Super-P C-particles. In some cases, polycrystalline Si regions are observed attached to the Si NPs (Figure 1a–c), due to the crystallization of the amorphous Si present in the starting material (see Figure S1, Supporting Information), during the pyrolysis process. Si NPs are surrounded by a few nm-thick SiO_2 shell (Figure 1c). Some Cu particles are found across the sample due to contamination from the current collector during the electrode preparation procedure.
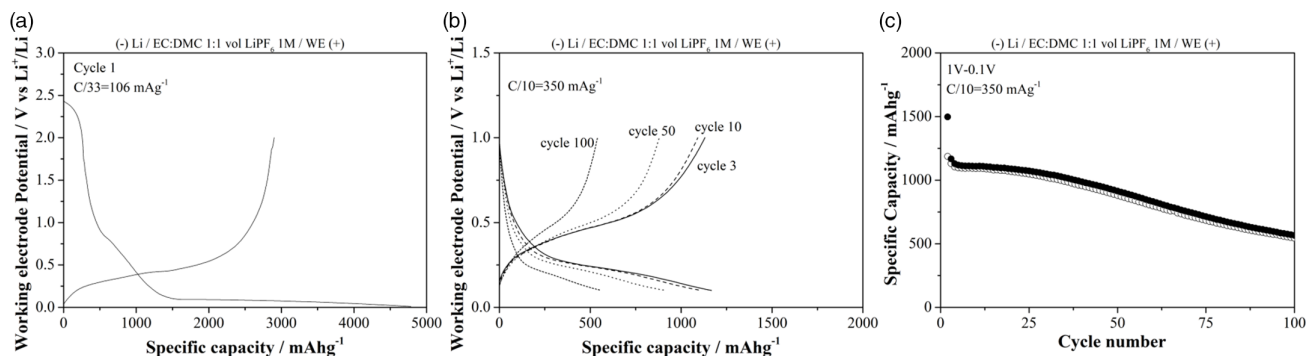
2.1. The Activation Cycle

Electrodes have been assembled in Li-half cells and tested in galvanostatic conditions: electrodes first underwent to an activation cycle in the 10 mV–2 V potential window, eventually followed by galvanostatic cycles in the 100 mV–1 V potential window. Postmortem analyses have been performed on electrodes, collected after cycling in both lithiated and delithiated states, by TEM and STEM.

The electrochemical performance of the Si-based electrodes is shown in **Figure 2**. As expected, the Si-based electrodes supply a large discharge capacity in the first electrochemical insertion (discharge branch of the activation cycle, Figure 2a)[12] reaching a Li loading corresponding to a nominal $Li_{4.98}Si$, well beyond the composition for the $Li_{15}Si_4$ or the $Li_{4.4}Si$ phases.[45] Approximately 1000 mAh g^{-1} are exchanged above 0.5 V versus Li^+/Li, largely due to parasitic reactions of the current collector and at the electrode/electrolyte interface (i.e., SEI formation).

TEM/STEM analyses of the Si electrodes after lithiation in the activation cycle show the alteration of the morphology and composition of the electrode materials. (Figure S2 and S3, Supporting Information). After the first activation lithiation,

Figure 1. a) TEM and b) STEM images of the as prepared electrode blend, showing crystalline Si NPs and C conductive fibres. Dark (a) and bright (b) small particles are related to copper. c) Isolated SiNPs surrounded by a thin SiO_2 layer on the right and polycrystalline Si on the left.

Figure 2. a) Working electrode potential curve of the activation cycle (first cycle at C/33) of the galvanostatic test; b) Working electrode potential profiles of the cycling at C/10; c) Specific capacities upon cycling at C/10.

large part of the Si NPs is mostly unaltered, showing a shape similar the pristine electrodes (see Figure 1 and S2, Supporting Information). Most of the Si NPs as well as the C-particles are enveloped in an organic/polymeric shell (Figure S3b, Supporting Information), not present in the pristine sample. This evidence demonstrates the precipitation of the SEI layer as consequence of electrolyte decomposition. Furthermore, many spherical particles are present throughout the entire lithiated electrode: these spherules are composed by Li, F, and O (Figure S4, Supporting Information). Large sheets, constituted by Li–F–P–O, are also found (Figure S3c, Supporting Information). Overall, electron microscopies and spectroscopies confirm that remarkable amounts of the exchanged capacity in the activation cycle originates from electrolyte decomposition and SEI formation, in consideration of the presence of large amount of almost unaltered Si NPs.

In the charge of the activation cycle a reversible capacity as large as 2904 mAh g^{-1} is exchanged, ending to a nominal composition after delithiation of Li$_{1.95}$Si (nominal capacity loss between discharge and charge 1850 mAh g^{-1}). This nominal composition overestimates the real Li trapping, in consideration of the capacity exchanged upon discharge above 0.5 V versus Li$^+$/Li. In this view, one may conclude that ≈46% of the capacity loss is related to Li trapping in the electrode and 54% to parasitic degradation reactions, thus matching the 1000 mAh g^{-1} discharge capacity above 0.5 V versus Li$^+$/Li. To confirm the large back conversion to metallic Si after the activation cycle, we recorded Raman spectra of electrodes recovered postmortem (see Figure S4, Supporting Information). Ex situ Raman spectroscopy confirms after activation the presence of crystalline Si together with amorphous Si, similarly to the pristine material. Turning to the additional electrode morphologies observed in the sample lithiated during the first activation discharge, the spherulites apparently disappear after the activation charge whereas the Li fluorophosphates sheets are still present after delithiation.

2.2. Electrochemical Performance After Activation

Once activated, the Si electrodes give a discharge capacity as large as 1500 mAh g^{-1}, and exchange a reversible capacity >1000 mAh g^{-1} for the firsts 30–35 cycle (Figure 2a,b). After cycle 35 the capacity fades smoothly with an average rate of −7 mAh g^{-1}

cycle to 580 mAh g^{-1} at cycle 100. The voltage profile upon cycling shows the expected symmetric sloping curve with a mean working potential of 0.7 V versus Li as other works the literature.[12]

Overall, the electrochemical performances in Li half cells highlight three different Li exchange regimes upon cycling: 1) the activation cycle, where ex situ TEM analyses indicate the occurrence of massive electrolyte decomposition and poor Si lithiation; 2) a stable capacity cycling between cycles 2 and 35; and 3) a constant capacity fading trend from cycle 35 to 100. Advanced electrochemical characterizations by galvanostatic intermitted titration tests (GITTs) highlight the occurrence of a large thermodynamic potential hysteresis between lithiation and delithiation in cells (see the Supplementary Note 2, Figure S5 and S6, Supporting Information). This behavior possibly originates from an asymmetry in the electrochemical process upon reduction and oxidation, similarly to conversion reaction electrodes.[46–48] The potential hysteresis is observed in the activation cycle as well as along the entire galvanostatic test. Remarkably, the diffusion coefficients of the Li ions in the silicon electrodes are approximately constant upon cycling (see the Figure S6, Supporting Information), thus demonstrating that the deactivation of the Si electrodes in the Li cells is not induced by a deterioration of electrode kinetics (e.g., hindered ionic transport in the solid state or at the electrolyte/electrode interphase) but more likely to deactivation mechanisms (e.g., active material loss).

It is noteworthy that the electrode deactivation is not apparently related neither to drastic alterations of the Li loading profile nor to changes in the redox mechanism, being the electrochemical fingerprint almost unaltered despite the smaller capacity exchanged at cycle 100 compared to cycle 10. To shed light in the Li exchange mechanism at the nanoscale, we carried out a detailed ex situ analysis by electron microscopy and nanoprobes of Si materials collected from cells after 10 cycles.

2.3. Electrode Morphologies and Composition After 10 Cycles (Lithiated State)

High angle annular dark field (HAADF) STEM images of the lithiated/discharged Si NPs after 10 cycles are shown in **Figure 3**. After lithiation, most of the pristine Si NPs are modified in shape and size (Figure 3a). These agglomerates have a pseudo-spherical
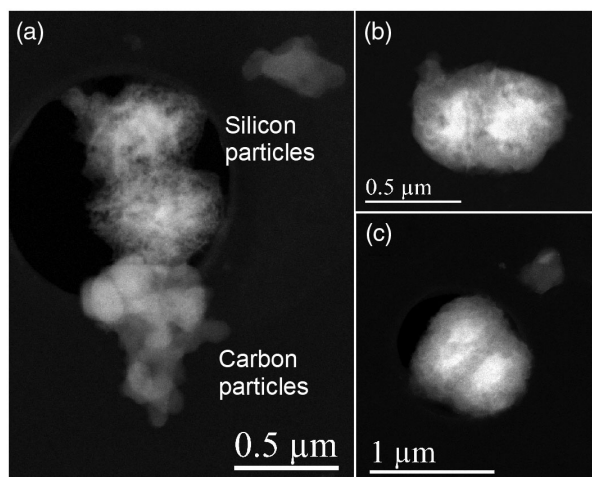
Figure 3. a-c) STEM images of three lithiated Si agglomerates after 10 cycles. The agglomerates are often composed of multipole starting Si NPs enveloped in the same shell.

shape with a diameter increased up to 400 nm. The foggy halo around a brighter core observed in the images point to a core-shell structure. Particles are typically sintered to form larger agglomerates (Figure 3b,c). Swollen C-particles are also detected, as reported in Figure 3a.

In parallel with the HAADF STEM image of one single agglomerate, shown in **Figure 4**a, point-by-point low and dual electron energy loss spectrum (EELS) spectrum have been acquired on the lithiated sample after 10 cycles. Three different EELS low loss signals are distributed across the agglomerate (Figure 4c): 1) the Si plasmon signal extracted from the Si NPs core (green); 2) the signal related to the conductive C-particles (red); 3) a complex signal coming from the outer shell (blue, see below for more details). The distribution maps of these three components, after multiple linear least square (MMLS) fitting procedure, are shown overlapped in the RGB image of Figure 4b and individually in Figure S7a–c, Supporting Information. The fitting results confirm the core–shell structure, with a Si core of 300 nm in diameter and an outer shell 100 nm thick. The outer shell is infiltrated by many Si filaments that show a plasmonic resonance at 16.4 eV typical of the amorphous Si^0 state (Figure S8, Supporting Information). Turning to the Li distribution at the nanoscale, low loss EELS Li signals are clearly detected inside the shell, in the C-particle whereas are very weak in the Si core only (see the inset in Figure 4c and S7d, Supporting Information). The low Li signal recorded from the Si core is likely due to the outer shell that surrounds the inner nucleus from above, although a weak contribution from the Si core cannot be completely excluded.

More information about the chemical composition of the outer shell is obtained from the high loss spectrum acquired simultaneously to the low loss ones. High loss EELS spectra have been sampled from shells of many agglomerates, in the energy range between 250 and 750 eV where C, O, and F signals are simultaneously recorded. F was rarely detected in the outer shell, while F edges have been recorded in the Li fluorophosphate sheets still present after 10 cycles (see Figure S3c, Supporting Information). The most common C and O edges detected across

the outer shell that surrounds the Si cores are shown in Figure 4 d, e. Their shapes suggest an attribution to Li carbonate, a common component of the SEI.[35] C and O, like in the low loss spectra, are uniformly distributed across the outer shell, indicating a homogeneous chemical composition throughout its thickness. Nevertheless, minor, and localized alterations at the outer surface and the inner interface cannot be fully excluded.

Overall, the lithiated Si NPs are composed of a Si core and a compact and uniform Li carbonate shell pervaded by Si filaments. It is important to mention that the Si plasmon peak from the Si NPs core is always centered at 16.4 eV. The Si plasmon is therefore only 0.4 eV shifted to lower energy compared with the literature crystalline Si as expected after an amorphous transition (see Figure S8, Supporting Information), and not from the presence of Li-rich Li_xSi alloys where the plasmon is down shifted to 13–15 eV. Nevertheless, these data do not exclude the possible dissolution of small amounts of Li in the amorphous Si lattice.

The absence of experimental evidence of Li-rich Li_xSi alloy in the lithiated samples do not fit with the expected lithiation mechanism, in consideration of the large experimental specific capacity recorded in the 10th discharge of the cell, i.e., 1100 mAh g^{-1}. Although this value is below the maximum theoretical capacity, it accounts for a nominal incorporation of 1.1 eq Li per Si atom: more details about the possible electrochemical mechanism are discussed below in Section 4.
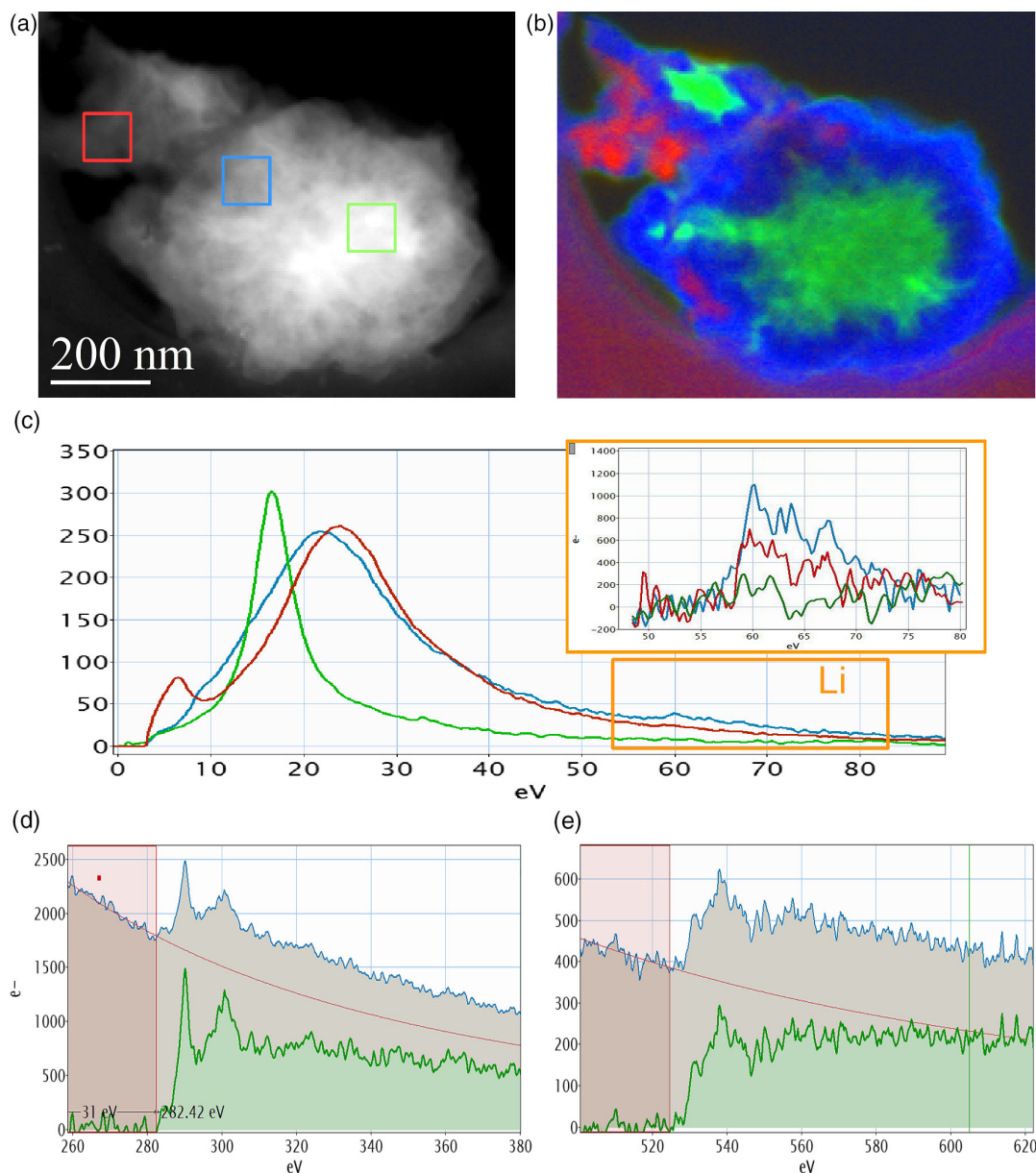
We would like to underline that a possible degradation of the air-sensitive lithiated samples before the STEM experiments must be excluded. First, accurate care has been paid in the loading of the STEM grids in Ar atmosphere using materials collected from cells never exposed to reactive environments (air, moisture, etc.). Second, the TEM grids have been preserved in coffee bags sealed under Ar until their insertion in the microscope. Third point, all the analyzed Si NPs were surrounded by a 100 nm-thick SEI layer that further protect the Si core by environmental effects.

2.4. Electrode Morphologies and Composition After 10 Cycles (Delithiated State)

The same morphological–compositional analysis at the nanoscale has been performed on the delithiated sample at cycle 10. In Figure S9, Supporting Information, dark field STEM images of Si agglomerates after delithiation are shown: the overall morphology appears similar to the lithiated sample, with a core–shell structure and a foggy contrast. However, the outer shell appears thinner and porous in the delithiated state compared with the lithiated one (Figure 3).

A representative dark field STEM image of one single delithiated agglomerate is shown in **Figure 5**a. The RGB composition, obtained after multiple linear least square (MLLS) fitting of the low loss spectrum image (SI, Figure 5b), using three contributions extracted from core, outer-shell and conductive C-particles is in line with the findings for the lithiated sample.

The most significant differences observed in the delithiated sample compared with the lithiated one is detected in the outer shell: 1) almost negligible Li signals and 2) a strong modification in the C and O high loss edges shape (Figure 5c,d). These two results prove an alteration of the composition of the outer-shell

**ADVANCED
SCIENCE NEWS**

www.advancedsciencenews.com

Energy Technology
Generation, Conversion, Storage, Distribution

www.entechnol.de

Figure 4. a) STEM dark field image of a lithiated Si agglomerate after 10 cycles. b) RGB distribution map after MLLS fitting (green: Si core; red: C agglomerates; blue: shell). c) Low loss signals used for MLLS fitting; in the inset Li signals are compared. High loss EELS: d) C and e) O edges samples in the outer shell.

upon delithiation, originating from the transformation of the lithium carbonate to an amorphous O-poor carbon material.

Turning to the inner nucleus, the Si plasmon resonance extracted from the core of the de-lithiated agglomerate holds at 16.4 eV, exactly as in the lithiated sample (Figure S8, Supporting Information). This value is commonly correlated with Si^0 species either crystalline or amorphous, in line with the findings from Raman spectroscopy (Figure S4, Supporting Information). This evidence proves a limited, if any, reactivity of the Si cores during lithiation/delithiation cycle at cycle 10.

The analysis of the spatial distribution of the atomic species in the outer shell around the Si NPs helps to outline some

additional insights concerning the composition of the SEI. The ionization edge maps visualize, in the same delithiated agglomerate of Figure 5, the C and O atomic distribution at the nanometer scale. In **Figure 6**a, we show an RGB image combining the Si distribution map from the MLLS fitting and C and O distributions from ionization edges (the individual components are shown in Figure S10, Supporting Information).

This combined map highlights a double-shell surrounding the inner Si core after delithiation: (outer shell, red) an O-poor thin C-layer; (inner shell, blue) a 10 nm-thick Si oxide layer; (core, green) a Si core. The SiO_2 formation is confirmed by the shape of the Si edge extracted from the inner blue shell, compared with
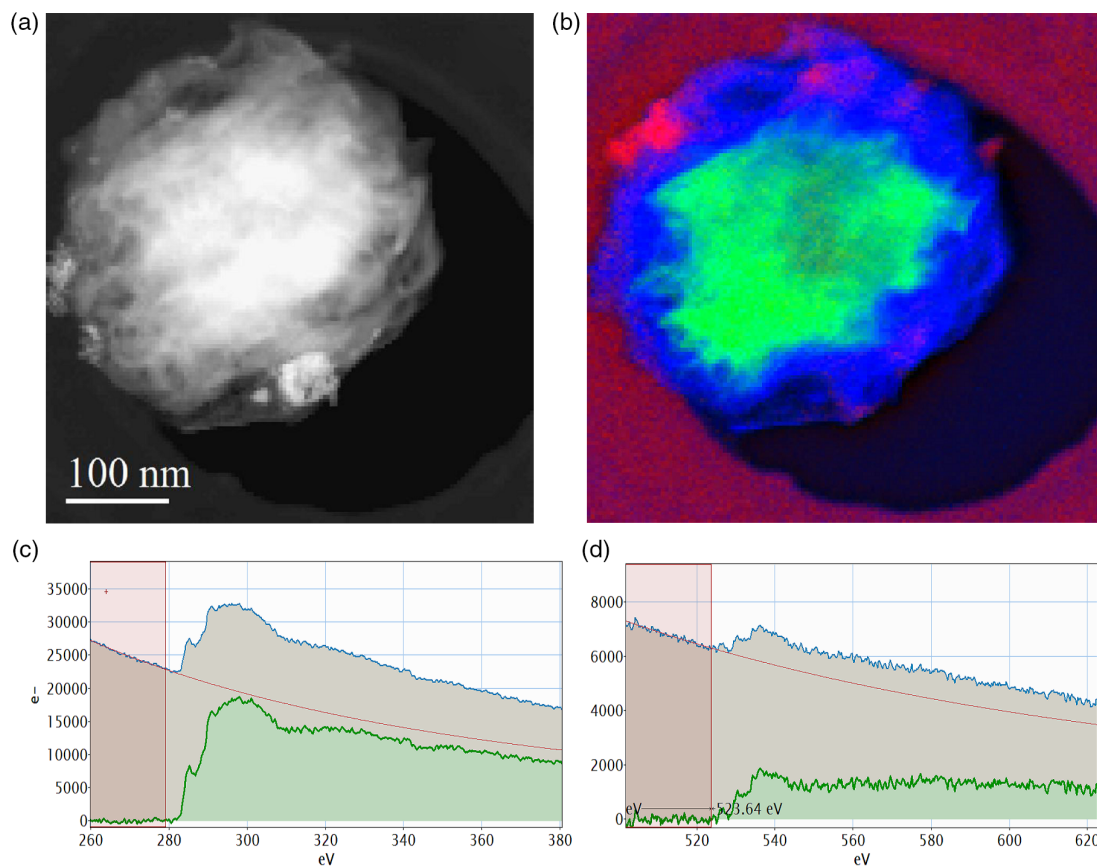
Figure 5. a) STEM dark field image of a delithiated Si agglomerate after 10 cycles. b) RGB distribution map from MLLS fitting. c) High loss EELS with C and d) O edges of the shell.
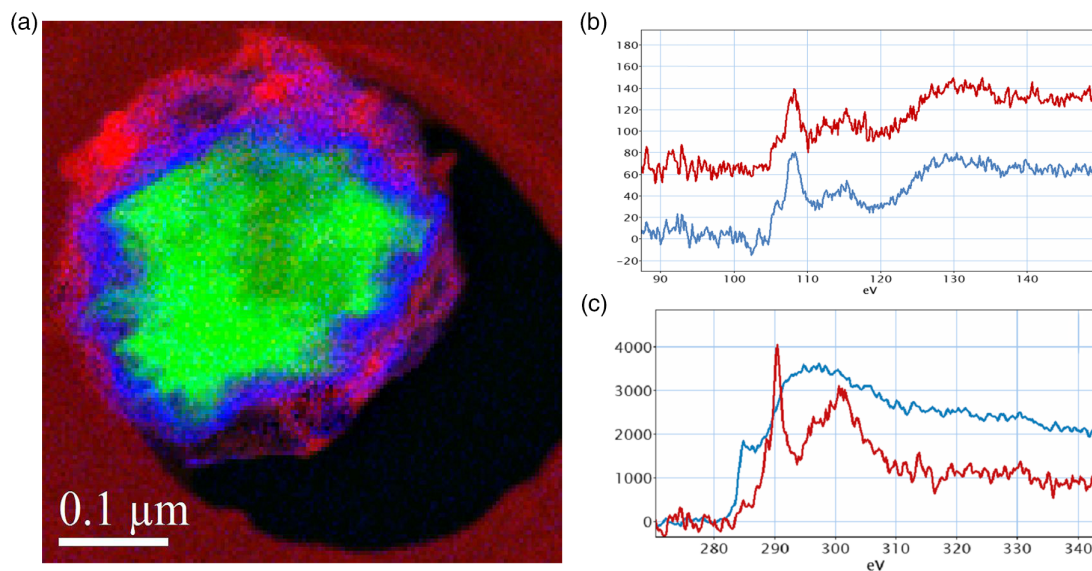
Figure 6. a) RGB image built with Si map from the MLLS fitting plus C and O maps derived by ionization edge (red: C; blue: O; green: Si). b) Si edge extracted from the inner blue shell (red) compared with reference SiO_2 (blue). c) C edge in lithiated (red) and delithiated (blue) shells.

a reference SiO_2 as shown in Figure 6b. The C edge measured from the outer C-rich/O-poor shell closely matches an amorphous C-layer and appears strongly modified compared with the Li_2CO_3 outer shell observed in the lithiated material.

The systematic analysis of many agglomerates observed in the delithiated sample confirms that most nanostructures show this double shell–core morphology: only few isolated Li_2CO_3 and LiF edge signals have been detected in very few Si NPs.

As expected, the Si electrodes are lithium deficient after delithiation, consistently with the electrochemical exchange of ≈ 1100 mAh g^{-1} in charge.

3. Discussion

Our experimental evidence highlights the alteration of the SEI composition during oxidation/reduction of Si-based electrodes even after 10 galvanostatic cycles in the cautious 0.1–1 V voltage range. The summary of compositions of Si electrodes obtained by Raman and EELS spectroscopies is in **Table 1**.
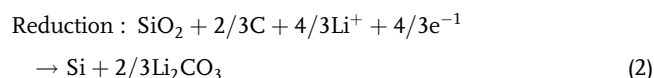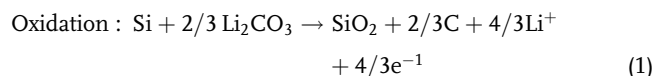
Our findings are in line with recent observation from refs. [22-25] where the possible occurrence an SEI-mediated electrochemical activity is proposed.

The morphological and compositional changes of the electrodes in the activation cycle are different compared to the reversible cycling. Apparently, the activation of the Si electrodes leads to limited changes in the elemental Si morphology, whereas the SEI layer undergoes to a significant compositional alteration: this phenomenon has been reported by many authors in the literature.[22–24,32] In this view, the large specific capacity is easily attributed to the SEI formation and only partially to the Li alloying in the amorphous Si.

After 10 galvanostatic cycles, the SEI-redox activity is still remarkable and possibly contributes to large fractions of the reversibly exchanged specific capacity of the whole electrode. In fact, during the 10th galvanostatic cycle, most Li$^+$ ions are stored within the SEI,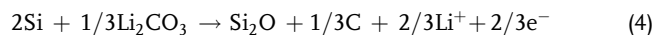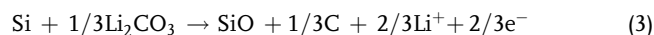 in the Li_2CO_3 outer shell, and not in the Si NPs cores. This lithium carbonate shell decomposes upon delithiation in parallel with the oxidation of the outer layers of the Si NPs, thus leading to a double shell (C/SiO_2) wrapping the Si cores in the delithiated state.

Starting from our experimental evidence, we can sketch a possible electrochemical mechanism involving the SEI to support the exchange of 1.14 Li eq per Si atom during the 10th galvanostatic cycle in a lithium half cells in parallel with a limited alloying in the amorphous Si. A first guess drafted directly from the species observed in the EELS patterns is

$$\text{Oxidation}: \ Si + 2/3\,Li_2CO_3 \rightarrow SiO_2 + 2/3C + 4/3Li^+ \\ + 4/3e^{-1} \quad (1)$$

$$\text{Reduction}: \ SiO_2 + 2/3C + 4/3Li^+ + 4/3e^{-1} \\ \rightarrow Si + 2/3Li_2CO_3 \quad (2)$$

However, simple thermodynamic considerations hinder this reaction, being the corresponding Nernst reduction potential $E°(SiO_2, C/Si, Li_2CO_3) = -0.79$ V versus Li^+/Li.[49]

Upon oxidation, one may take into account also the possible metastable formation of amorphous non-stoichiometric Si–O phases like SiO and Si_2O through the following reactions[50]

$$Si + 1/3Li_2CO_3 \rightarrow SiO + 1/3C + 2/3Li^+ + 2/3e^- \quad (3)$$

$$2Si + 1/3Li_2CO_3 \rightarrow Si_2O + 1/3C + 2/3Li^+ + 2/3e^- \quad (4)$$

The corresponding Nernst reduction potential at 298 K are: $E°(SiO, C/Si, Li_2CO_3) = -0.43$ V versus Li^+/Li and $E°(Si_2O, C/Si, Li_2CO_3) = 0.60$ V versus Li^+/Li. Thus, thermodynamics allows upon oxidation reaction R4 above 0.60 V versus Li^+/Li.[51]

Table 1. Experimental identification of morphologies/phases/composition in the Si electrodes.

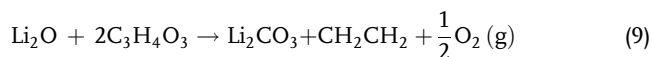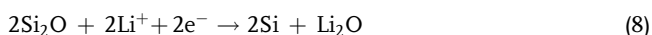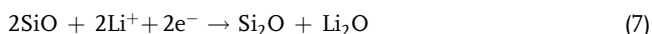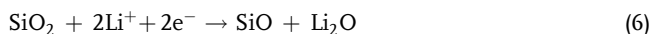| State of discharge/charge		Raman spectroscopy	TEM/STEM	EELS spectroscopy
Pristine		Si(crystalline)	Si NPs	
		Si(amorphous)	C rounded particles	
			Cu fragments	
			α-Si layers	
			SiO_x layers	
Activation cycle	End of discharge (lithiated/reduced)		Si NPs	LiF
			$LiF/Li_xO_yF_z$ spherules	$Li_xO_yF_z$
			Li-oxyfluorophosphate sheets	$Li_aP_bO_cF_d$
			C-layer	
	End of the activation cycle (delithiated/oxidized)	Si(crystalline)	Si NPs	$Li_aP_bO_cF_d$
		Si(amorphous)	Li-oxyfluorophosphate sheets	
Cycling	10th end of discharge (lithiated/reduced)		Si NPs with dendritic outer shells	Si(amorphous)
			Swollen C-particles	Li_2CO_3
	10th end of charge (delithiated/oxidized)	Si(amorphous)	Si NPs with dendritic outer shells	Si(amorphous)
		Organic compounds	Swollen C-particles	O-poor carbons
				SiO_2
				Li_2CO_3
				LiF

Once formed, Si_2O can easily undergo to a thermodynamically driven oxidation mediated by the organic carbonates. As an example, one may consider the reaction of Si_2O with ethylene carbonate ($C_3H_4O_3$) to give SiO_2, C, and gaseous ethylene

$$Si_2O + C_3H_4O_3 \rightarrow 2SiO_2 + C + CH_2CH_2(g) \tag{5}$$
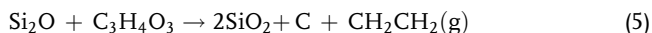
Reaction (R5) is strongly exergonic with a Gibbs energy of reaction at 298 K of $-1029\,kJ\,mol^{-1}$ and may easily drive the transformation of the amorphous Si_2O to SiO_2.[52,53] We would like to stress that the combination of (R4) and (R5) is a possible example of a thermodynamically reasonable path to drive the electrochemical oxidation of Si to SiO_2 mediated by the SEI. Our hypothesis is consistent with our experimental observations but is not necessarily the only one occurring. Moreover, this specific Si^0/Si^{4+} electrochemical/chemical reaction path is irreversible and therefore a different mechanism is required to electrochemically discharge the composite electrodes to drive the reduction of SiO_2 to lithium carbonate and metallic Si. This electrochemical asymmetry matches our findings in the GITT tests (see above).

Few combinations of thermodynamically driven electrochemical and chemical reactions that can, in principle, support the exchange of large specific capacity through a similar irreversible mechanism mediated by the SEI layer are

$$SiO_2 + 2Li^+ + 2e^- \rightarrow SiO + Li_2O \tag{6}$$

$$2SiO + 2Li^+ + 2e^- \rightarrow Si_2O + Li_2O \tag{7}$$

$$2Si_2O + 2Li^+ + 2e^- \rightarrow 2Si + Li_2O \tag{8}$$

$$Li_2O + 2C_3H_4O_3 \rightarrow Li_2CO_3 + CH_2CH_2 + \frac{1}{2}O_2\,(g) \tag{9}$$

The electrochemical sequence (R6)–(R7)–(R8) has Nernst reduction potentials at 298 K of 0.58, 0.47, and 1.73 V versus Li+/Li, respectively, whereas the chemical reaction of Li oxide with ethylene carbonate to give lithium carbonate, acetylene, and molecular O_2 is an exergonic process with Gibbs energy of reaction at 298 K of $-226\,kJ\,mol^{-1}$.

We would like to underline that both reaction sequences, (R6)–(R7)–(R8)–(R9) upon lithiation and (R4)–(R5) upon delithiation, matches with our experimental evidences. A full validation of this complex process that wastes the electrolyte and release of ethylene and molecular O_2 requires an experimental approach beyond the goal of this work and needs gas-sampling analytical techniques beyond our capabilities.

As a final comment, we would like to underline that a fully reversible redox activity involving the formation of organic by-products is unlikely as well as a full reversible reduction of SiO_2. Thus, the final consideration is that the available reactive Si is consumed cycle-by-cycle. In fact, upon oxidation the SiO_2 layer acts as a barrier that limits Si oxidation after reaching a critical thickness, thus limiting overall reversibility. On the other hand, the reduction process works very effectively on nanosized Si where the exposed surface is maximized and, thus an effective lithium carbonate reduction to a C-rich material occurs. Both processes, i.e., oxidation and reduction, exploit/cause the Si dendritization upon cycling, thus leading to a decrease the Si core radius and an increase the amount of lithium carbonate formed

in the interstices. The pristine Si cores are continuously consumed upon cycling until the full dissolution and, afterwards, all the transformations are assisted only by the available Si filaments distributed inside the large agglomerate.

4. Conclusions

A detailed morphological and spectroscopic analysis at the nanoscale of the alteration of Si NPs in Li cells has been reported. In summary even cycling in the cautious 0.1–1 V versus Li voltage range, the electrochemical reactions that supports the Li^+ incorporation/deincorporation in Si-based electrodes can also originate to a vast oxidation/reduction from Si^0 to Si^{4+} mediated by lithium carbonate and amorphous C. Thus, the redox activity of Si in Li-cells is strongly interplayed with the concurrent degradation chemistry of the solvent molecules in the electrolyte.

Furthermore, the reversible Si oxidation/reduction process at the Si NPs interface with the SEI, drive and support irreversible redox reactions that drive the metallic Si dendritization and pulverization. Overall, this mechanism damages, cycle-by-cycle, the morphological integrity of the Si NPs by surface erosion during oxidation and segregation during reduction, resulting in the formation of thin filament inside the shell. Consequently, upon cycling the electrochemical performance necessarily changes in parallel with the accumulation of degradation by-products and the exhaustion of Si metallic centers.

5. Experimental Section

Si NPs Synthesis: An inductively coupled plasma chemical vapor deposition (ICP-CVD) system was used in Si NPs synthesis. In the experimental setup, Ar gas was flown through a cylinder and was excited by radio frequency (RF). The use of high-density plasma ($2/6 \times 10^{11}$ ions cm^{-3}) had the advantage of requiring low substrate temperature and low gas fluxes. An argon-silane (Ar-SiH$_4$) gas mixture was formed at low pressures in a cylindrical reaction chamber with 6 inches of diameter. Radio-frequency power of 500 W at 13.56 MHz was applied through a matching network to two copper ring electrodes. The reflected power was below 1.5% of the forward power. Base pressure was $<5 \times 10^{-6}$ Torr. Typical flow rates were 20 sccm for SiH$_4$ and 1 sccm for Ar that was used just to ignite the plasma. Si NPs were synthesized in the plasma through electron impact dissociation of SiH$_4$ and subsequent reactions.[58] After nucleation, the Si NPs were let to grow until the plasma was switched-off and fall on the substrate.[59,60] The process time was set to 45 s although such long time was not related to Si NPs nucleation, which was generally of few milliseconds, but it was needed to let them to grow in the plasma.[61,62]

Electrode Preparation and Electrochemical Testing: The Si-based electrode tapes were obtained by drop casting followed by consolidation at high temperature in controlled gas flow. The Si active material was dispersed in *N*-methyl pyrrolidone (NMP, Sigma Aldrich) by ultrasonication (Solution A with concentration 8.33 mg$_{Si}$ mL^{-1}). The conductive additive, i.e., SuperP carbon (Timcal) and the polymeric binder (polyacrylic acid, PAA, Sigma Aldrich) were both dispersed as well in NMP, namely solution B and C with identical concentration of 25 mg mL^{-1}. A 3:1:1 volume ratio of the solutions A, B, and C were ultrasonicated for 60 min and then casted on precut carbon-coated copper disks of 14 mm in diameters (MTI Corp) with a controlled Si loading of 0.25 mg cm^{-2}. NMP was evaporated in two steps: 1) 6 h at room temperature followed by 2) 9 h at 70 °C in static oven. Dried electrodes have been transferred in alumina liners and inserted in a tubular furnace for pyrolysis/consolidation (MTI Corp). Annealing conditions were optimized to achieve minimal oxidation and optimal consolidation of the active material as follow: Ar flow at 120 mL min^{-1}, heating

ramp at $0.5\,°C\,min^{-1}$ followed by a 30 min rest at 650 °C and natural cooling. The obtained electrodes were collected, further dried under vacuum for 8 h at 120 °C (Buchi tubular oven) and then transferred in an Ar-filled glovebox (Iteco Eng SGS30) with moisture contamination below 0.1 ppm.

Electrodes were assembled in Li half-cells by coupling the working electrode with a Whatman fiberglass separator and Li counter electrode. A standard 1 M $LiPF_6$ EC:DMC 1:1 vol (Solvionic) was used as electrolyte ($25\,mL\,cm^{-2}$). ECC-Std cells were used as outer cases for Li half cells to facilitate the electrode collection after cycling. Cell manufacture were carried out in an Iteco SGS30 Ar-filled glovebox with moisture level below 0.1 ppm. Cells were submitted to galvanostatic cycling (GC) experiments to evaluate the performance of the active material: current rates were set by assuming $1C = 3500\,mA\,g^{-1}$. For all materials, the GC procedures implied one discharge/charge activation step with voltage cutoffs at 10 mV and 2 V (activation cycle), respectively, followed by discharge/charge cycles in the 0.1–1 V range. Coulombic efficiencies were calculated by the ratio between the charge and the discharge capacity obtained for a given cycle number. GC were carried out using an 8-channel MTI battery cycling system: cells temperature was carefully controlled at 25 °C by using a Memmert static oven. Galvanostatic intermitting titration tests were carried out by a sequence of galvanostatic pulses at C/33 for 30 min followed by 6 h at open-circuit condition to achieve thermodynamic equilibrium: working electrode potential cutoffs at 0.1 V in discharge and 1 V in charge were adopted whereas discharge-to-charge current inversion was set after 66 pulses, thus limiting the capacity to theoretical value. Li-ion diffusion coefficients were calculated from GITT using the standard equations.[63]

Ex Situ Investigation Methods and Techniques: As prepared and working electrodes after 10 GC tests were collected for ex situ analyses. Cells were transferred back in glovebox and disassembled. The collected electrodes were carefully washed in dimethyl carbonate (Sigma Aldrich, dried under molecular sieves) and tetrahydrofuran (Sigma Aldrich, dried under molecular sieves) to remove the salt traces and all soluble contaminants from the electrode. Washed electrodes were dried under dynamic vacuum for 30 min and then stored in glove box. C-coated Cu grids for TEM investigation of electrode materials were prepared in glovebox from THF suspension of active materials recuperated from cells. Once loaded TEM grids were stored in holders and sealed under Ar in coffee bags to preserve their integrity from moisture and air contamination before insertion in the TEM apparatus.

Scanning transmission electron microscopy analyses were performed with a JEOL ARM200C at 200 keV. Electron energy loss spectroscopic data were collected using a GATAN Quantum EEL spectrometer. EELS SIs were acquired in dual EELS mode, with parallel acquisition of low and high loss spectra, together with HAADF signal. Low beam current and very fast point acquisitions were used in order to avoid macroscopic changes on the samples. Every spectrum of the image was aligned using the zero-loss peak and then deconvoluted for plural scattering subtraction. The plural scattering deconvolution process allowed a standardization of the low loss spectra, independently by the thickness, necessary condition for the correct application of the MLLS fitting. MLLS fitting was used on the deconvoluted low loss dataset, using as reference three main spectra extracted from the same SI, as described in the text. Elemental maps were extracted from the aligned high loss SI using inner ionization edge after background subtraction. Plural scattering deconvolution, MLLS fitting, and all the data analysis were performed using the Gatan Microscopy suite v3.01.

Raman analysis was performed using a Dilor LabRam confocal micro-Raman spectrometer utilizing a HeNe 632.8 nm 4.7 mW laser, an 1800 grooves mm^{-1} grating, and a $50\times$ objective.

The X-ray diffraction (XRD) experiment was carried out at the MCX beamline at ELETTRA synchrotron radiation source (=1.033 Å): the diffraction pattern was recorded in the 15°–60° 2θ range with steps of 0.02° (time/step of 3 s).

Scanning electron micrographs have been recorded by using a field emission scanning electron microscope (FESEM) at the CNIS research centre (ZEIS Auriga).

Supporting Information

Supporting Information is available from the Wiley Online Library or from the author.

Conflict of Interest

The authors declare no conflict of interest.

Data Availability Statement

The data that support the findings of this study are available from the corresponding author upon reasonable request.

[1] J. M. Tarascon, M. Armand, *Nature* **2001**, 414.

[2] B. Scrosati, J. Garche, *J. Power Sources* **2010**, 195.

[3] J. M. Tarascon, *Nat. Chem.* **2010**, *2*, 510.

[4] K. Ozawa, *Lithium Ion Rechargeable Batteries*, Wiley-VCH, Weinheim **2009**.

[5] F. Bonino, S. Brutti, M. Piana, S. Natale, B. Scrosati, L. Gherghel, K. Müllen, *Electrochim. Acta* **2006**, *51*, 3407.

[6] M. Agostini, S. Brutti, J. Hassoun, *ACS Appl. Mater. Interfaces* **2016**, *8*, 10850.

[7] J. Sun, G. Zheng, H. W. Lee, N. Liu, H. Wang, H. Yao, W. Yang, Y. Cui, *Nano Lett.* **2014**, *14*, 4573.

[8] C. M. Park, J. H. Kim, H. Kim, H. J. Sohn, *Chem. Soc. Rev.* **2010**, *39*, 3115.

[9] M. Zeilinger, I. M. Kurylyshyn, U. Häussermann, T. F. Fässler, *Chem. Mater.* **2013**, *25*, 4623.

[10] D. Ma, Z. Cao, A. Hu, *Nano-Micro Lett.* **2014**, *6*, 347.

[11] J. Wang, T. Xu, X. Huang, H. Li, T. Ma, *RSC Adv.* **2016**, *6*, 87778.

[12] J. R. Szczech, S. Jin, *Energy Environ. Sci.* **2011**, *4*, 56.

[13] M. R. Zamfir, H. T. Nguyen, E. Moyen, Y. H. Lee, D. Pribat, *J. Mater. Chem. A* **2013**, *1*, 9566.

[14] R. Zhou, H. Guo, Y. Yang, Z. Wang, X. Li, Y. Zhou, *Powder Technol.* **2016**, *295*, 296.

[15] C. Fu, C. Song, L. Liu, W. Zhao, X. Xie, *Int. J. Electrochem. Sci.* **2016**, *11*, 154.

[16] T. D. Bogart, D. Oka, X. Lu, M. Gu, C. Wang, B. A. Korgel, *ACS Nano* **2014**, *8*, 915.

[17] A. Magasinski, B. Zdyrko, I. Kovalenko, B. Hertzberg, R. Burtovyy, C. F. Huebner, T. F. Fuller, I. Luzinov, G. Yushin, *ACS Appl. Mater. Interfaces* **2010**, *2*, 3004.

[18] X. H. Liu, L. Zhong, S. Huang, S. X. Mao, T. Zhu, J. Y. Huang, *ACS Nano* **2012**, *6*, 1522.

[19] U. Kasavajjula, C. Wang, A. J. Appleby, *J. Power Sources* **2007**, *163*, 1003.

[20] M. T. McDowell, I. Ryu, S. W. Lee, C. Wang, W. D. Nix, Y. Cui, *Adv. Mater.* **2012**, *24*, 6034.

[21] M. T. McDowell, S. W. Lee, W. D. Nix, Y. Cui, *Adv. Mater.* **2013**, *25*, 4966.

[22] N. Dupré, P. Moreau, E. De Vito, L. Quazuguel, M. Boniface, A. Bordes, C. Rudisch, P. Bayle-Guillemaud, D. Guyomard, *Chem. Mater.* **2016**, *28*, 2557.

[23] M. Boniface, L. Quazuguel, J. Danet, D. Guyomard, P. Moreau, P. Bayle-Guillemaud, *Nano Lett.* **2016**, *16*, 7381.

[24] M. Wetjen, S. Solchenbach, D. Pritzl, J. Hou, V. Tileli, H. A. Gasteiger, *J. Electrochem. Soc.* **2018**, *165*, A1503.

[25] K. Ogata, S. Jeon, D. S. Ko, I. S. Jung, J. H. Kim, K. Ito, Y. Kubo, K. Takei, S. Saito, Y. H. Cho, H. Park, J. Jang, H. G. Kim, J. H. Kim, Y. S. Kim, W. Choi, M. Koh, K. Uosaki, S. G. Doo, Y. Hwang, S. Han, *Nat. Commun.* **2018**, *9*, 479.

[26] M. Wetjen, D. Pritzl, R. Jung, S. Solchenbach, R. Ghadimi, H. A. Gasteiger, *J. Electrochem. Soc.* **2017**, *164*, A2840.

[27] Y. Jin, B. Zhu, Z. Lu, N. Liu, J. Zhu, *Adv. Energy Mater.* **2017**, *7*, 1.

[28] H. Gao, L. Xiao, I. Plümel, G. L. Xu, Y. Ren, X. Zuo, Y. Liu, C. Schulz, H. Wiggers, K. Amine, Z. Chen, *Nano Lett.* **2017**, *17*, 1512.

[29] M. N. Obrovac, L. Christensen, *Electrochem. Solid-State Lett.* **2004**, *7*, A93.

[30] P. Lu, C. Li, E. W. Schneider, S. J. Harris, *J. Phys. Chem. C* **2014**, *118*, 896.

[31] P. B. Balbuena, Y. Wang, *Lithium-Ion Batteries: Solid-Electrolyte Interphase*, Imperial College Press, London **2004**.

[32] E. Peled, D. Golodnitsky, G. Ardel, *J. Electrochem. Soc.* **1997**, *144*, L208.

[33] P. Verma, P. Maire, P. Novák, *Electrochim. Acta* **2010**, *55*, 6332.

[34] K. Guo, R. Kumar, X. Xiao, B. W. Sheldon, H. Gao, *Nano Energy* **2020**, *68*, 104257.

[35] M. Sina, J. Alvarado, H. Shobukawa, C. Alexander, V. Manichev, L. Feldman, T. Gustafsson, K. J. Stevenson, Y. S. Meng, *Adv. Mater. Interfaces* **2016**, *3*, 1.

[36] S. Benning, C. Chen, R. A. Eichel, P. H. L. Notten, F. Hausen, *ACS Appl. Energy Mater.* **2019**, *2*, 6761.

[37] G. M. Veith, M. Doucet, R. L. Sacci, B. Vacaliuc, J. K. Baldwin, J. F. Browning, *Sci. Rep.* **2017**, *7*, 1.

[38] T. Kennedy, M. Brandon, F. Laffir, K. M. Ryan, *J. Power Sources* **2017**, *359*, 601.

[39] W. Huang, J. Wang, M. R. Braun, Z. Zhang, Y. Li, D. T. Boyle, P. C. McIntyre, Y. Cui, *Matter* **2019**, *1*, 1232.

[40] C. Cao, I. I. Abate, E. Sivonxay, B. Shyam, C. Jia, B. Moritz, T. P. Devereaux, K. A. Persson, H. G. Steinrück, M. F. Toney, *Joule* **2019**, *3*, 762.

[41] C. Cao, H. G. Steinrück, B. Shyam, M. F. Toney, *Adv. Mater. Interfaces* **2017**, *4*, 1.

[42] M. Miyachi, H. Yamamoto, H. Kawai, T. Ohta, M. Shirakata, *J. Electrochem. Soc.* **2005**, *152*, A2089.

[43] G. Lener, M. Otero, D. E. Barraco, E. P. M. Leiva, *Electrochim. Acta* **2018**, *259*, 1053.

[44] W. S. Chang, C. M. Park, J. H. Kim, Y. U. Kim, G. Jeong, H. J. Sohn, *Energy Environ. Sci.* **2012**, *5*, 6895.

[45] R. Tamori, N. Machida, T. Shigematsu, *Funtai Oyobi Fummatsu Yakin/J. Jpn. Soc. Powder Powder Metall.* **2001**, *48*, 267.

[46] A. L. Dalverny, J. S. Filhol, M. L. Doublet, *J. Mater. Chem.* **2011**, *21*, 10134.

[47] R. Khatib, A. L. Dalverny, M. Saubaneàre, M. Gaberscek, M. L. Doublet, *J. Phys. Chem. C* **2013**, *117*, 837.

[48] D. Meggiolaro, G. Gigli, A. Paolone, P. Reale, M. L. Doublet, S. Brutti, *J. Phys. Chem. C* **2015**, *119*, 17044.

[49] M. W. Chase, C. A. Davies, J. R. Downey, D. J. Frurip, R. A. McDonald, A. N. Syverud, *NIST-JANAF Thermochemical Tables*, Standard Reference Data Program National Institute of Standards and Technology, Gaithersburg, MD **1985**.

[50] M. Riera, J. A. Rodríguez, J. Barreto, C. Domínguez, **2007**, *515*, 3380.

[51] M. Nagamori, J. Boivin, A. Claveau, **1995**, *189*, 270.

[52] J. C. Chao, B. J. Zwolinski, *J. Phys. Chem Ref. Data*, **1975**, *4*, 251.

[53] K. G. Joback, R. C. Reid, *Chem. Eng. Commun.*, **1987**, *57*, 233.

[54] L. Ravi, S. L. Girshick, *Phys. Rev. E - Stat. Nonlinear, Soft Matter Phys.* **2009**, *79*, 1.

[55] G. Faraci, A. R. Pennisi, A. Alberti, R. Ruggeri, G. Mannino, *Sci. Rep.* **2015**, *5*, 8354.

[56] G. Mannino, A. Alberti, R. Ruggeri, S. Libertino, A. R. Pennisi, G. Faraci, *Scientific Reports* **2015**, *5*, 1.

[57] E. M. L. D. De Jong, G. Mannino, A. Alberti, R. Ruggeri, M. Italia, F. Zontone, Y. Chushkin, A. R. Pennisi, T. Gregorkiewicz, G. Faraci, *Scientific Reports* **2016**, *6*, 25664.

[58] G. Faraci, M. Italia, R. Ruggeri, G. Litrico, G. Mannino, *J. Raman Spectrosc.* **2019**, *50*, 674.

[59] C. Ho, I. D. Raistrick, R. A. Huggins, *J. Electrochem. Soc.* **1980**, *127*, 343.